On the black hole mass of the γ-ray emitting narrow-line Seyfert 1 galaxy 1H 0323+342

H. Landt,[1]$\star$ M. J. Ward,[1] M. Baloković,[2] D. Kynoch,[1] T. Storchi-Bergmann,[3] C. Boisson,[4] C. Done,[1,5] J. Schimoia[3] and D. Stern[6]

[1]*Department of Physics, Centre for Extragalactic Astronomy, Durham University, South Road, Durham DH1 3LE, UK*
[2]*Cahill Center for Astronomy and Astrophysics, California Institute of Technology, 1216 E California Blvd, Pasadena, CA 91125, USA*
[3]*Departamento de Astronomia, Universidade Federal do Rio Grande do Sul, IF, CP 15051, 91501-970 Porto Alegre, RS, Brazil*
[4]*LUTH, Observatoire de Paris, CNRS, Université Paris Diderot, PSL Research University Paris, 5 place Jules Janssen, F-92195 Meudon, France*
[5]*ISAS, Japan Aerospace Exploration Agency, 3-1-1 Yoshinodai, chuo-ku, Sagamihara, Kanagawa 252-5210, Japan*
[6]*Jet Propulsion Laboratory, California Institute of Technology, 4800 Oak Grove Drive, Pasadena, CA 91109, USA*

ABSTRACT

Narrow-line Seyfert 1 galaxies have been identified by the *Fermi Gamma-Ray Space Telescope* as a rare class of γ-ray emitting active galactic nuclei. The lowest redshift candidate among them is the source 1H 0323+342. Here we present quasi-simultaneous *Gemini* near-infrared and *Keck* optical spectroscopy for it, from which we derive a black hole mass based on both the broad Balmer and Paschen emission lines. We supplement these observations with a *Nuclear Spectroscopic Telescope Array* X-ray spectrum taken about two years earlier, from which we constrain the black hole mass based on the short time-scale spectral variability. Our multiwavelength observations suggest a black hole mass of $\sim 2 \times 10^7$ M$_\odot$, which agrees well with previous estimates. We build the spectral energy distribution and show that it is dominated by the thermal and reprocessed emission from the accretion disc rather than the non-thermal jet component. A detailed spectral fitting with the energy-conserving accretion disc model of Done et al. constrains the Eddington ratio to $L/L_{\rm Edd} \sim 0.5$ for a (non-rotating) Schwarzschild black hole and to $L/L_{\rm Edd} \sim 1$ for a Kerr black hole with dimensionless spin of $a^\star = 0.8$. Higher spin values and so higher Eddington ratios are excluded, since they would strongly overpredict the observed soft X-ray flux.

Key words: quasars: emission lines – quasars: individual: 1H 0323+342 – galaxies: Seyfert – infrared: galaxies – X-rays: galaxies.

1 INTRODUCTION

The majority of γ-ray emitting active galactic nuclei (AGN) discovered by the *Fermi Gamma-Ray Space Telescope* and listed in its third Large Area Telescope catalogue (Acero et al. 2015) are blazars, evenly distributed between flat-spectrum radio quasars and BL Lacertae objects. However, a very small number of γ-ray emitting AGN are optically classified as narrow-line Seyfert 1s, i.e. they have much lower optical luminosities than quasars and their broad emission lines are relatively narrow with full widths at half-maximum (FWHM) $\lesssim 2000$ km s^{-1}. They usually also have very strong emission lines from permitted Fe II transitions in their optical spectra (Boroson & Green 1992). Since the first discovery of γ-ray emitting narrow-line Seyfert 1s (Abdo et al. 2009), only eight sources are known to date (Foschini et al.

2016). All of these sources are radio-loud and their γ-ray emission is thought to be produced via the external Compton mechanism whereby the relativistic jet electrons upscatter a photon field external to the jet, e.g. from the accretion disc, broad emission-line region (BLR) or dusty torus, to higher energies. This interpretation is also often used to explain the γ-ray emission detected from broad-line quasars.

The discovery of narrow-line Seyfert 1s as a class of γ-ray emitting AGN is intriguing, since they generally reside in spiral galaxies rather than in bright ellipticals that are usually the hosts of radio-loud AGN with powerful relativistic jets. Furthermore, as a class, the narrow-line Seyfert 1s tend to have lower black hole masses and higher accretion rates relative to their Eddington limit compared with the typical Seyfert 1 AGN. This means that the thermal accretion disc spectrum and its Comptonized components are expected to dominate over the jet emission at optical/UV wavelengths and X-ray energies. This dominance is rarely seen over this entire frequency range in the other γ-ray emitting blazar classes and so these sources

$\star$ E-mail: hermine.landt@durham.ac.uk

offer us the unique opportunity to study the connection between jet and accretion power.

Among the γ-ray detected narrow-line Seyfert 1s, the source 1H 0323+342 is of particular interest, since it has the lowest redshift ($z = 0.0629$; Zhou et al. 2007). This not only means that its host galaxy can be resolved by ground-based imaging (Antón, Browne & Marchã 2008; León Tavares et al. 2014) and that due to its relatively high-flux good signal-to-noise (S/N) ratio observations can be obtained in relatively short exposure times, but also that its black hole mass can be reliably estimated from single-epoch spectra using several broad emission lines. Its optical spectrum covers simultaneously the two strongest Balmer lines, Hα and Hβ, both for which reliable black hole mass scaling relations exist (e.g. Greene & Ho 2005; Bentz et al. 2009; Xiao et al. 2011; Bentz et al. 2013) and a cross-dispersed near-infrared (near-IR) spectrum with its large wavelength coverage gives simultaneous observations of the two strongest Paschen lines, Paα and Paβ, for which a black hole mass scaling relation has recently been presented by Landt et al. (2011a, 2013). The black hole mass is a key ingredient for modelling the accretion disc spectrum that, in turn, determines the accretion power relative to the Eddington limit and the bolometric luminosity.

Here we present recent quasi-simultaneous optical and near-IR spectroscopy of high quality (high S/N and moderate spectral resolution), from which we derive a black hole mass based on both the broad Balmer and Paschen emission lines. We supplement these observations with a *Nuclear Spectroscopic Telescope Array (NuSTAR)* X-ray spectrum taken about two years earlier, from which we constrain the black hole mass based on the short time-scale spectral variability. This paper is organized as follows. In Section 2, we describe the near-IR, optical and X-ray observations based on which we estimate the black hole mass as detailed in Section 3. In Section 4, we construct the multiwavelength spectral energy distribution (SED), which we fit with the energy-conserving accretion disc model of Done et al. (2012, 2013) in order to constrain the Eddington ratio. Finally, in Section 5, we summarize our main results and present our conclusions. Throughout this paper, we have assumed cosmological parameters $H_0 = 70$ km s^{-1} Mpc^{-1}, $\Omega_{\rm M} = 0.3$ and $\Omega_\Lambda = 0.7$. Photon spectral indices have been defined as $N(E) \propto E^{-\Gamma}$.

2 THE OBSERVATIONS

2.1 The near-IR spectroscopy

We observed the source 1H 0323+342 in queue mode with the *Gemini* Near-Infrared Spectrograph (GNIRS; Elias et al. 2006) at the *Gemini* North 8 m observatory in semester 2015B (Program ID: GN-2015B-FT-4) in the framework of the recently initiated Fast Turnaround Program. The observations were taken on 2015 September 16. There were no clouds and the seeing was excellent. We used the cross-dispersed mode with the short camera at the lowest resolution (31.7 l mm^{-1} grating), thus covering the entire wavelength range of 0.9–2.5 µm without inter-order contamination. We chose a slit of 0.45 arcsec × 7 arcsec. This set-up gives an average spectral resolution of FWHM ∼265 km s^{-1}. The on-source exposure time was 6 × 90 s at an average airmass of sec $z = 1.037$, which resulted in an average continuum S/N ∼ 40, 70 and 90 in the *J*, *H* and *K* bands, respectively. Since the source is too extended for the relatively small slit length, we nodded off on to a blank patch of sky for the background subtraction.

Before the science target, we observed the nearby (in position and air mass) A2 V star HIP 16168 that has accurate near-IR magnitudes. We used this standard star to correct our science spectrum for telluric absorption and for flux calibration. Flats and arcs were taken after the science target. The data were reduced using the *Gemini*/IRAF package (version 1.13) with GNIRS specific tools (Cooke & Rodgers 2005). The data reduction steps included preparation of calibration and science frames, processing and extraction of spectra from science frames, wavelength calibration of spectra, telluric correction and flux-calibration of spectra and merging of the different orders into a single, continuous spectrum. The spectral extraction width was adjusted interactively for the telluric standard star and the science source to include all the flux in the spectral trace. The final spectrum was corrected for Galactic extinction using the IRAF task *onedspec.deredden* with an input value of $A_{\rm V} = 0.706$, which we derived from the Galactic hydrogen column densities published by Dickey & Lockman (1990). The result is shown in Fig. A1.

2.2 The optical spectroscopy

We obtained an optical spectrum of the source 1H 0323+342 on 2016 February 14, with the Low Resolution Imaging Spectrometer (LRIS; Oke et al. 1995) mounted on the *Keck* 10 m telescope. The weather was photometric with a seeing of ∼0.6 arcsec. We used the 600/4000 and 400/8500 gratings for the blue and red arms, respectively, with the 1 arcsec slit. This set-up gives a relatively large spectral coverage of ∼3100–10 300 Å, with a very small spectral gap of ∼40 Å between the two arms. The average spectral resolution is FWHM ∼300 km s^{-1}, similar to that of our near-IR spectroscopy. The slit was rotated to the parallactic angle, but note that the LRIS has an atmospheric dispersion corrector. The on-source exposure time was 300 s at an average airmass of sec $z = 1.65$, which resulted in an average continuum S/N ∼ 60. The data were reduced using standard longslit routines from the IRAF software package. The extracted spectrum was flux-calibrated using the standard stars G191B2B and HZ 44 with fluxes as given in Massey & Gronwall (1990). The final spectrum was corrected for Galactic extinction as was done for the near-IR spectrum (see Section 2.1). The result is shown in Fig. A2. We note that based on the observed wavelength of the forbidden narrow emission lines and narrow components of the broad emission lines in both our near-IR and optical spectra, we get a redshift of $z = 0.0625$, which differs by ∼120 km s^{-1} from the value of $z = 0.0629$ published by Zhou et al. (2007). At the spectral resolution of our data, this difference is significant, since the wavelength position of the emission line peak can be determined with sub-pixel accuracy.

The optical and near-IR spectrum have a considerable wavelength region of overlap at their respective red and blue ends, which we can use to test if the source flux has varied between the two observing epochs. Importantly, this overlap wavelength region covers the strong forbidden narrow emission line [S III]λ9531. For this line, we measure an integrated flux of 1.25×10^{-15} and 8.92×10^{-16} erg s^{-1} cm^{-2} for the near-IR and optical spectrum, respectively. The difference in continuum flux in the overlap wavelength region is similar (∼40 per cent), with the optical spectrum having again a lower flux than the near-IR spectrum. Therefore, flux calibration issues rather than genuine source variability are favoured as the cause for the flux misalignment between the two spectra. In order to further check the absolute flux calibration of the optical spectrum, we have compared the flux of the strong forbidden narrow emission line [O III]λ5007 to that observed in the optical spectrum published by Marchã et al. (1996). Their spectrum was obtained in

1992 November with the Multiple Mirror Telescope (MMT) 4.5 m on Mt. Hopkins, Arizona, USA, using a 1.5 arcsec slit oriented at parallactic angle and the 150 l mm^{-1} grating. This set-up resulted in a spectral resolution of ~1200 km s^{-1} over the wavelength range of ~3770–8683 Å. After correcting the MMT spectrum for Galactic reddening and subtracting the Fe II emission in both spectra as described in Section 3.1, we measure an integrated flux of 1.06 × 10^{-14} and 1.50 × 10^{-14} erg s^{-1} cm^{-2} for the [O III]λ5007 line in the *Keck* and MMT optical spectrum, respectively. The difference between the two is ~40 per cent, similar to what we found when comparing the *Keck* optical spectrum with our near-IR spectrum. Therefore, for the following analysis, we have scaled the optical spectrum up to the flux level of the near-IR spectrum. We note that Berton et al. (2016) have also recently obtained an optical spectrum. The [O III]λ5007 line luminosity that they measure in their 2014/15 spectrum from the Asiago 1.2 m telescope is ~10 per cent lower than our measurement in the *Keck* spectrum.

2.3 The X-ray spectroscopy

2.3.1 NuSTAR

The source 1H 0323+342 was observed with the *NuSTAR* (Harrison et al. 2013) between 2014 March 15 and 18 for a total duration of 198.72 ks. We processed the data using the NUPIPELINE script available in NUSTARDAS version 1.4.1 (HEASOFT version 1.16) with the calibration database CALDB version 20150316. Occasional high count rates were filtered out using the SAA=Strict filter, reducing the total exposure time by ≲10 per cent. The sum of good-time intervals after event cleaning and filtering is 91 ks for both focal plane modules A (FPMA) and B (FPMB). For each module, we extracted source spectra from circular regions with 60 arcsec radius centred on the peak of the emission, while the background spectra were extracted from source-free regions of the same detector, towards the edge of the field of view. Background accounts for ≲6 per cent of the counts in the source region within the 3–79 keV bandpass. We obtain an S/N ~ 100 and ~70 per module for the 3–10 and 10–79 keV bands, respectively.

Source spectra, light curves and response files were generated using the NUPRODUCTS script. The light curves for the energy bands 3–10 and 10–79 keV are shown in Fig. A3, top panel. We used a time binning of 30 min in order to have at least two time bins per *NuSTAR* orbit (of ≃90 min). We omitted bins containing less than 3 min of source exposure. The point spread function-corrected total source count rate was fluctuating around 0.33 cts s^{-1}, except for a short period near the middle of the observation when it flared up to ≃0.5 cts s^{-1}. In Fig. A3, bottom panel, we show the hardness ratio as a function of time to demonstrate that the spectrum did not significantly change during this brief period of increased flux. For the X-ray spectral analysis, we describe in the following we used the time-averaged spectra binned to a minimum of 50 counts per energy bin. For the analysis of the SED in Section 4, we co-added the FPMA and FPMB spectra using standard HEASOFT FTOOLS and used 12 wide energy bins over the total 3–79 keV band to aid visibility in Fig. 2.

We first analysed the two *NuSTAR* spectra separately using XSPEC (Arnaud 1996). We fitted the FPMA and FPMB spectra simultaneously, without co-adding. We assumed the following three models: a single power law, a log-parabolic model ($F(E) \propto E^{-\alpha - \beta \log E}$) and the sum of two power laws. All models assumed a fixed redshift for the source of $z = 0.0625$, a fixed Galactic hydrogen column density of $N_H = 14.62 \times 10^{20}$ cm^{-2} (Dickey & Lockman 1990) and a

cross-normalization factor, which was allowed to vary in the spectral fits. We selected the best-fitting model by requiring an *F*-test probability >99.99 per cent so that the χ^2 value of the model with the larger number of free parameters represents an improvement. We found that a single power law model fits the data best, with $\chi^2 = 575.1$ for 515 dof giving a reduced χ^2 value of $\chi^2_\nu = 1.12$. The best-fit photon index for this model is $\Gamma = 1.80 \pm 0.01$, where the uncertainty is given as the 1σ confidence interval. The resulting 2–10 keV flux is 8.10 × 10^{-12} erg s^{-1} cm^{-2}. Replacing the power-law continuum with the more flexible log-parabolic model or the sum of two power laws does not give a statistically significant improvement. We obtain a $\chi^2 = 568.6$ for 514 dof and a $\chi^2 = 568.6$ for 513 dof for the former and latter model, respectively, resulting in *F*-test probabilities of 98.4 per cent and 94.6 per cent, respectively. However, it is worth mentioning that the fit with two power-laws gives spectral indices of $\Gamma_1 \sim 2$ and $\Gamma_2 \sim 1.2$–1.6 below and above a break energy of $E_{break} \sim 25$ keV, respectively, which correspond well to the typical photon indices for coronal and jet contributions observed in the X-ray spectra of Seyferts, in particular of narrow-line Seyfert 1s (see also Section 4.2).

We have tested the data for the presence of other spectral features commonly observed in the hard X-ray spectra of AGN, namely, the Compton hump and the iron line at 6.4 keV, by adding two components to the power-law continuum. We used the pexrav model (Magdziarz & Zdziarski 1995) to represent the reprocessed continuum with most parameters fixed (high-energy cutoff at 1 MeV, inclination at 60°, elemental abundances at Solar values), and a narrow, unresolved Gaussian to represent the emission line. We find that the contributions of these two components are small and that this model does not constitute a statistically significant improvement in comparison to the single power law ($\chi^2 = 567.6$ for 513 dof, resulting in an *F*-test probability of 96.6 per cent). Finally, we note that for all models, we find that the cross-normalization factor (FPMB/FPMA) is 1.06 ± 0.02, which is on the high side but still within expectations from *NuSTAR* calibration (Madsen et al. 2015).

2.3.2 Swift

Since our near-IR/optical spectroscopy and the *NuSTAR* X-ray spectrum are separated in time by about two years, we have used archival *Swift* observations, which have simultaneous optical/UV magnitudes and X-ray spectra, to check for extreme flux variability between the two epochs. *Swift* observed the source 1H 0323+342 on 2015 September 17, i.e. only one day after the near-IR spectroscopy was taken, but there are no observations very close in time with the *NuSTAR* spectroscopy. Therefore, we have used those two *Swift* observations that are the closest in time with it, namely, the data taken on 2013 August 20 and 2014 December 10, i.e. about seven months earlier and about nine months later, respectively. Within the *Swift* archive, we used data collected with the X-ray Telescope (XRT) in photon counting mode. We reprocessed the initial event files with the XRTPIPELINE (version 0.13.2) using standard settings and the latest known calibration files. Source spectra were extracted from circular regions corresponding to an encircled energy of ~90 per cent at 1.5 keV. Background spectra were taken from a circular region with a radius roughly three times as large as that of the source and offset from the source position. The background-subtracted spectra were fit using XSPEC, with the response matrices from the calibration database. The source spectra were binned to a minimum of 20 counts per energy bin in order to apply the χ^2 minimization

Table 1. *Swift* XRT and UVOT observations.

Observation date	ObsID	Exposure (s)	Source counts	Γ	$f_{(2-10\mathrm{keV})}$ (erg s^{-1} cm^{-2})	χ_ν^2/dof
(1)	(2)	(3)	(4)	(5)	(6)	(7)
2013 August 20	00036533044	3798	1222	1.96 ± 0.05	8.35e−12	0.80/52
2014 December 10	00036533052	2972	1365	1.94 ± 0.05	1.10e−11	0.95/59
2015 September 17	00036533064	1636	670	1.99 ± 0.08	9.79e−12	0.98/30

Observation date	V (mag)	B (mag)	U (mag)	$UVW1$ (mag)	$UVM2$ (mag)	$UVW2$ (mag)
(1)	(8)	(9)	(10)	(11)	(12)	(13)
2013 August 20	15.62 ± 0.06	16.10 ± 0.04	15.24 ± 0.04	15.36 ± 0.05	15.71 ± 0.07	15.55 ± 0.05
2014 December 10	15.51 ± 0.05	16.02 ± 0.04	15.09 ± 0.04	15.38 ± 0.05	15.74 ± 0.06	15.70 ± 0.05
2015 September 17	15.70 ± 0.09	16.25 ± 0.06	15.35 ± 0.06	15.57 ± 0.08	15.78 ± 0.09	15.78 ± 0.07

Notes. The columns are: (1) date of observation; (2) observation ID; for the XRT X-ray observations (3) filtered live exposure time; (4) extracted source counts; (5) photon index; (6) observed flux in the range of 2–10 keV; and (7) reduced χ^2 and number of degrees of freedom for a single power law fit with a fixed Galactic hydrogen column density of $N_{\mathrm{H}} = 14.62 \times 10^{20}$ cm^{-2}; for the simultaneous UVOT observations, the observed (absorbed) Vega magnitudes in the (8) V filter ($\lambda_{\mathrm{eff}} = 5402$ Å), (9) B filter ($\lambda_{\mathrm{eff}} = 4329$ Å), (10) U filter ($\lambda_{\mathrm{eff}} = 3501$ Å), (11) $UVW1$ filter ($\lambda_{\mathrm{eff}} = 2634$ Å), (12) $UVM2$ filter ($\lambda_{\mathrm{eff}} = 2231$ Å) and (13) $UVW2$ filter ($\lambda_{\mathrm{eff}} = 2030$ Å). We quote all errors at the 1σ level.

technique. We fit the data with two different models, namely, a single power law and a broken power law. The hydrogen column density was fixed to the Galactic value and in the case of the single power law fits also allowed to vary. The best-fitting model was, in all cases, a single power law with a fixed Galactic hydrogen column density. The relevant parameter values for the X-ray fits together with the simultaneous optical/UV magnitudes from the Ultraviolet Optical Telescope (UVOT) on-board *Swift* are reported in Table 1.

We find that the *Swift* X-ray flux in the 2–10 keV energy range changed by ∼30 per cent between the two observing epochs before and after the *NuSTAR* X-ray spectroscopy, with the earlier epoch having a very similar X-ray flux to the *NuSTAR* spectrum and the later one a value only ∼10 per cent higher than the observing epoch close in time with the near-IR spectroscopy. Furthermore, the average between the two is very similar to the X-ray flux of the observing epoch corresponding to the near-IR spectrum. Neither is a strong flux variability observed in the optical/UV. Significant flux changes are detected in the B, U, $UVW1$ and $UVW2$ filters, but only by ∼20–30 per cent at the 2–3σ level. Therefore, we have co-added the three *Swift* X-ray spectra and performed again the spectral fits. This time, the best-fitting model was a broken power law with a fixed Galactic hydrogen column density ($\chi_\nu^2 = 0.87$ for 124 dof), showing clearly the soft X-ray excess typical of narrow-line Seyfert 1s in addition to the hard power law. The resultant spectral indices in the soft and hard X-ray bands are $\Gamma_{\mathrm{soft}} = 2.22^{+0.06}_{-0.05}$ and $\Gamma_{\mathrm{hard}} = 1.72^{+0.10}_{-0.12}$, respectively, for a break energy of $E_{\mathrm{break}} = 2.04^{+0.41}_{-0.31}$ keV. The 0.3–10 keV flux is 1.69×10^{-11} erg s^{-1} cm^{-2}, which points at the source being in a high state and intermediate between the first and second flare investigated by Paliya et al. (2014) in their 2008–2013 *Swift* XRT light curve (see their table 5).

3 ESTIMATES OF THE BLACK HOLE MASS

In this section, we estimate the black hole mass in the source 1H 0323+342 using two different quantities that scale with it, namely, the virial product between the width of a broad emission line and the continuum luminosity, which serves as a proxy for the BLR radius, and the short time-scale variability in the X-ray band. The first method assumes that the dynamics of the gas in the BLR is dominated by gravitational forces and uses the virial theorem to calculate the black hole mass as:

$$M_{\mathrm{BH}} = f \frac{R \Delta V^2}{G}, \tag{1}$$

where R is the radial distance of the BLR gas from the black hole, ΔV is the velocity dispersion of the gas, G is the gravitational constant and f is a scaling factor that depends on the (unknown) dynamics and geometry of the BLR. The BLR radius can be directly measured through reverberation mapping, a technique that determines the light-travel time-delayed lag with which the flux of the BLR responds to changes in the ionizing continuum flux. However, since reverberation mapping campaigns are observing time intensive, the so-called radius–luminosity relationship is used to estimate the BLR sizes for large samples of AGN from single-epoch spectra. As has been shown (e.g. Peterson 1993; Wandel, Peterson & Malkan 1999; Kaspi et al. 2000; Bentz et al. 2009; Landt et al. 2011a), the BLR lags obtained from reverberation mapping campaigns correlate with the optical, UV and near-IR luminosity (of the ionizing component) largely as expected from simple photoionization arguments.

The second method assumes that the X-ray variability properties, such as time-scales and amplitude, of all sources (galactic and extragalactic) that host a black hole are determined by its mass; the larger the black hole mass, the larger the size of the X-ray emitting region and so the longer the time-scales on which the X-ray emission varies, leading to smaller variability amplitudes (Barr & Mushotzky 1986; Green, McHardy & Lehto 1993; Nandra et al. 1997; McHardy et al. 2006).

3.1 Near-IR and optical spectroscopy

We first estimate the black hole mass using the near-IR relationship presented by Landt et al. (2013). This relationship is based on the virial product between the 1 μm continuum luminosity and the width (FWHM or line dispersion) of the strongest Paschen broad emission lines, Paα or Paβ. As detailed by these authors, the main advantage of the near-IR virial product over the optical one is the reliable measurement of its quantities; both Paα and Paβ are observed to be unblended and the continuum around 1 μm is free of major contaminating components. Host galaxy starlight has its emission maximum at ∼1 μm, but its contribution is usually negligible in
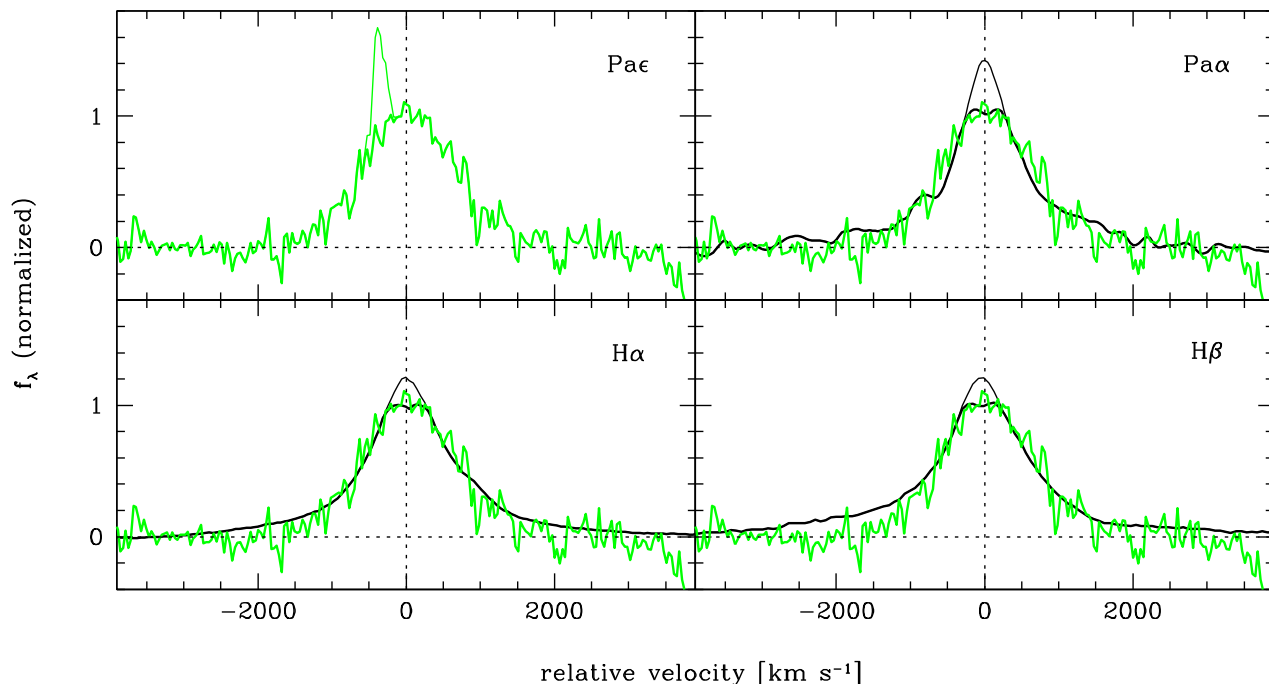
Figure 1. The profile of the Pa ε emission line (thick green lines in upper left panel; here taken from the *Keck* LRIS optical spectrum) is blended with the forbidden narrow emission line [S III]λ9531 (thin green lines) but its narrow component is absent. After removing the largest possible flux contribution from the narrow emission-line region (thin black lines), the resulting profile of the broad component of the Paα, Hα and Hβ emission lines (thick black lines in upper right, lower left and lower right panels, respectively) is similar to that of the Pa ε emission line (thick green lines).

luminous AGN if the near-IR spectrum was obtained through a small slit. In our case, we can estimate the host galaxy flux at 1μm enclosed by our spectral aperture using the imaging results of León Tavares et al. (2014). These authors give surface brightness estimates in the *R* band for both a bulge and a bulge plus disc model of the host galaxy, which we use to scale the S0 galaxy template of Polletta et al. (2007). In this way, we estimate that the luminosity of the host galaxy at 1μm in our near-IR spectrum lies a factor of ≳70 below the total luminosity.

The *Gemini* GNIRS near-IR spectrum covers simultaneously both the Paα and Paβ emission lines as well as the rest-frame 1 μm wavelength region. However, the Paβ emission line is strongly affected by atmospheric absorption since it lies at the end of the atmospheric window. Therefore, in the following, we estimate the black hole mass using only the Paα broad emission line, for which we measure the linewidth as the FWHM, i.e. we use specifically equation 2 in Landt et al. (2013). The measurement of the 1 μm continuum luminosity is straightforward and we get a value of $\log \nu L_{1\mu m} = 43.92$ erg s^{-1}. However, in order to correctly measure the width of the Paα broad component, we need to first separate it from the narrow component. Based on absent narrow components observed for the higher order Paschen emission lines, Landt et al. (2014) have suggested that the correct approach to this is to subtract the largest possible flux contribution from the narrow emission-line region. This contribution is obtained by first estimating the FWHM of a strong forbidden narrow emission line and then fitting a Gaussian of this width to the top part of the total emission line profile. We have applied this method here and show the result in Fig. 1. In the source 1H 0323+342, we find that already the Pa ε emission line, which is blended with the strong forbidden narrow emission line [S III]λ9531, has no narrow component (thick green line in Fig. 1, upper left panel). A Gaussian fit to the [O III]λ5007 emission line observed in the optical spectrum gives an FWHM = 294 km s^{-1}.

Subtracting a Gaussian with this width from the top part of the total Paα emission line (thin black lines) leaves a broad component with a similar profile to that observed for the Pa ε emission line (Fig. 1, upper right panel). We measure an FWHM = 1120 km s^{-1} for the Paα broad component, which results in a black hole mass of $(2.0^{+0.8}_{-0.6}) \times 10^7$ solar masses (see also Table 2).

We next estimate the black hole mass using the latest scaling relations based on the optical virial product between the ionizing 5100 Å continuum luminosity and the width of the strongest Balmer broad emission lines Hα and Hβ. All these three quantities are covered simultaneously by our *Keck* LRIS optical spectrum. The measurement of the 5100 Å continuum luminosity is straightforward and we get a value of $\log \nu L_{5100\,\text{Å}} = 44.05$ erg s^{-1} (in the scaled-up spectrum as described in Section 2.2). After subtracting the narrow component of the Hα emission line in a similar way as we did for the Paα emission line (Fig. 1, lower left panel), we measure an FWHM = 1412 km s^{-1} for the Hα broad component. Using the recently recalibrated black hole mass relationship of Mejía-Restrepo et al. (2016), specifically the calibration for the local continuum fit corrected for small systematic offsets (see their table 7), we estimate the black hole mass to be $(1.5^{+0.7}_{-0.5}) \times 10^7$ solar masses (see also Table 2).

As is typical for narrow-line Seyfert 1 galaxies, the emission from permitted Fe II transitions is very strong in the source 1H 0323+342. This emission needs to be modelled and subtracted in order to reliably measure the width of the Hβ emission line, since the numerous optical Fe II multiplets form a pseudo-continuum around the line and blend in with its red wing. We used the template based on the optical spectrum of I Zw 1 published by Véron-Cetty, Joly & Véron (2004) and available in electronic format to model and subtract the Fe II emission. The method generally used to subtract the Fe II emission from optical spectra was first introduced by Boroson & Green (1992). It consists of creating a spectral sequence by broadening (by

Table 2. Estimates of the black hole mass using different methods.

Wavelength	Measurements	$M_{\rm BH}$ $(10^7\,{\rm M_\odot})$	Reference
Near-IR	$\log \nu L_{1\,\mu m} = 43.92$ erg s^{-1} FWHM(Paα) = 1120 km s^{-1}	$2.0^{+0.8}_{-0.6}$	Equation 2 of Landt et al. (2013)
Near-IR	$\log \nu L_{1\,\mu m} = 43.92$ erg s^{-1} σ(Paα) = 875 km s^{-1}	$1.8^{+1.3}_{-0.7}$	Equation 3 of Landt et al. (2013)
Near-IR	$\log L_{\rm Pa\,\alpha} = 41.46$ erg s^{-1} FWHM(Paα) = 1120 km s^{-1}	1.0 ± 0.2	Equation 9 of Kim, Im & Kim (2010)
Optical	$\log \nu L_{5100\,\text{Å}} = 44.05$ erg s^{-1} FWHM(Hα) = 1412 km s^{-1}	$1.5^{+0.7}_{-0.5}$^{a}	Table 7 of Mejía-Restrepo et al. (2016)
Optical	$\log L_{\rm H\,\alpha} = 42.44$ erg s^{-1} FWHM(Hα) = 1412 km s^{-1}	$0.6^{+0.4}_{-0.2}$^{a}	Table 7 of Mejía-Restrepo et al. (2016)
Optical	$\log \nu L_{5100\,\text{Å}} = 44.05$ erg s^{-1} FWHM(Hβ) = 1437 km s^{-1}	$2.2^{+0.8}_{-0.6}$^{a}	Table 14 of Bentz et al. (2013)
Optical	$\log L_{\rm H\,\beta} = 42.02$ erg s^{-1} FWHM(Hβ) = 1437 km s^{-1}	$1.2^{+0.8}_{-0.5}$^{a}	Table 2 of Greene et al. (2010)
X-ray/ optical	$\log L_{2-10\,\rm keV} = 43.97$ erg s^{-1} FWHM(Hβ) = 1437 km s^{-1}	$2.2^{+1.8}_{-1.0}$^{a}	Table 2 of Greene et al. (2010)
X-ray	$\sigma^2_{\rm rms} = 0.007 \pm 0.005$ (20 ks)	$1.0^{+3.3}_{-0.5}$^{b}	Table 3 of Ponti et al. (2012)
X-ray	$\sigma^2_{\rm rms} = 0.005 \pm 0.003$ (40 ks)	$1.7^{+3.3}_{-0.8}$^{b}	Table 3 of Ponti et al. (2012)

^{a}The 1σ error is derived from the instrinsic scatter rather than the errors on the best-fitting parameter values.
^{b}The 1σ error includes the measurement errors in addition to the errors on the best-fitting parameter values.

convolution with Gaussians) and scaling of the Fe II template, which is subsequently packed together into a three-dimensional cube. This cube is then subtracted from a cube consisting in all three dimensions of the object's spectrum. But, as noted by Landt et al. (2008) and Vestergaard & Peterson (2005), it can be rather difficult to decide by eye unambiguously which pair of width and strength of the Fe II template gives the cleanest subtraction, and so it is necessary to constrain a priori the width of the Fe II template. Following Landt et al. (2008), we have done this by using the width of the unblended near-IR iron emission line Fe II 1.0502 μm. For this, we measure a value of FWHM = 1034 km s^{-1}, which is similar to the linewidth of FWHM = 1100 km s^{-1} used for the Fe II template. Therefore, in this case we did not need to broaden the Fe II template but only to scale it. In this way, we achieved a satisfactory Fe II subtraction around the Hβ line. After subtracting its narrow component in a similar way as we did for the Hα and Paα emission lines (Fig. 1, lower right panel), we measure an FWHM = 1437 km s^{-1} for the Hβ broad component. Using the radius–luminosity relationship for the Hβ line of Bentz et al. (2013) derived from optical reverberation mapping results, specifically their calibration 'Clean2+ExtCorr' cleaned for bad time lags and corrected for internal extinction (see their table 14), and assuming a geometrical scaling factor of $f = 1.4$ appropriate for FWHM measures (Onken et al. 2004), we derive a black hole mass of $(2.2^{+0.8}_{-0.6}) \times 10^7$ solar masses (see also Table 2).

3.2 X-ray variability

The short time-scale X-ray variability is best quantified by deriving the power density spectrum and determining its amplitude and break frequency, i.e. the frequency at which the spectral slope changes. But such an analysis is very difficult with unevenly sampled data as afforded by low-Earth orbit satellites such as *NuSTAR*. Therefore, we have considered here instead the normalized excess variance, $\sigma_{\rm rms}$, which was first introduced by Nandra et al. (1997) as an X-ray variability measure. This quantity has been shown to correlate well with black hole mass, most recently by Ponti et al. (2012) who used data obtained with *XMM–Newton*. Because the bandpasses of

XMM–Newton and *NuSTAR* differ, count rates of the former are dominated by low-energy photons. However, considering only the 3–10 keV band of *NuSTAR*, the differences are minimized and we assume that the scaling relations hold for variability statistics based on *NuSTAR* count rates as well.

We have computed the 3–10 keV light curve (see Fig. A3) and calculated the normalized excess variance and its 1σ error following Vaughan et al. (2003) using segments of total length of 20 and 40 ks. Averaging between FPMA and FPMB, we obtain values of $\sigma^2_{\rm rms} = 0.007 \pm 0.005$ and 0.005 ± 0.003 for the 20 and 40 ks cases, respectively. Using the relationships between $\sigma^2_{\rm rms}$ and black hole mass published by Ponti et al. (2012) for their reverberation-mapped AGN sample and listed in their table 3, we obtain a black hole mass of $(1.0^{+3.3}_{-0.5}) \times 10^7$ and $(1.7^{+3.3}_{-0.8}) \times 10^7$ solar masses for the 20 and 40 ks cases, respectively (see also Table 2). These values are in good agreement with our results from the near-IR and optical spectroscopy presented above. However, if we use instead the relationships for their entire sample and listed in their table 5, we obtain considerably larger values, namely, a black hole mass of 2.1×10^7 and 4.3×10^7 solar masses for the 20 and 40 ks binning, respectively. In particular, the latter value is inconsistent with our near-IR/optical spectroscopy results. However, we note that our *NuSTAR* light curve has a time binning of 30 min to minimize the impact of the orbit gaps and maximize S/N, but this means that compared to the 250 s binning used by Ponti et al. (2012), we may underestimate the excess variance and so overestimate the black hole mass.

3.3 Discussion

Our three estimates of the black hole mass in the source 1H 0323+342 based on the ionizing continuum luminosity and the width of an hydrogen broad emission line give a very small range of values of $\sim$1.5–2.2 $\times$ 10^7 solar masses, with an average value of $\sim$2 $\times$ 10^7 solar masses. This excellent agreement between the three estimates is surprising, given that the relationships upon which they are based have uncertainties of the order of $\sim$40–50 per cent
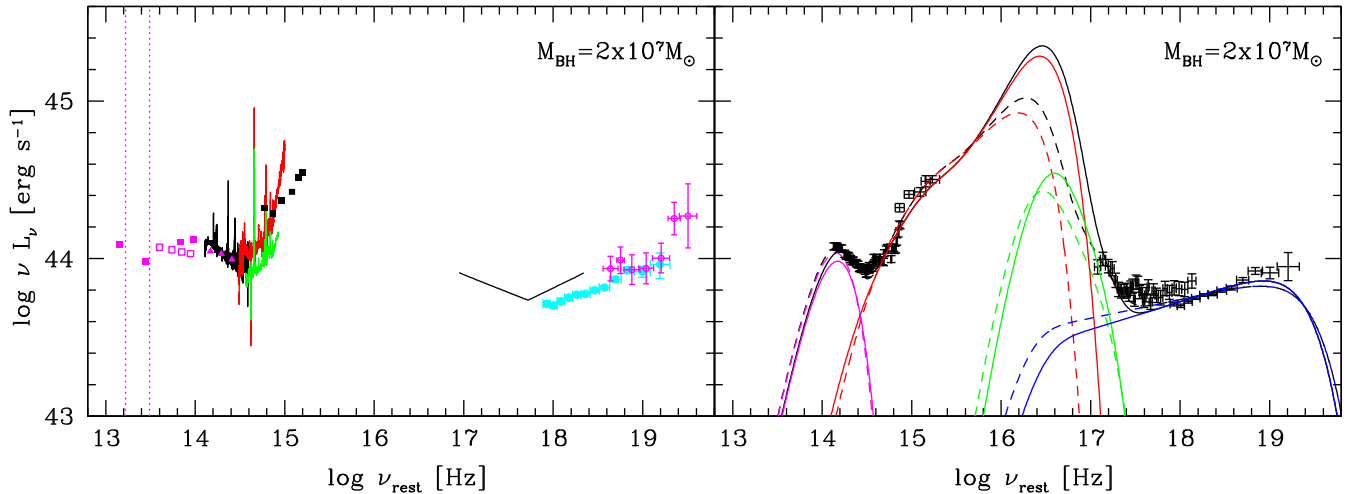
Figure 2. Left-hand panel: rest-frame spectral energy distribution for the source 1H 0323+342 based on *Gemini* GNIRS near-IR spectroscopy (black solid line), *Keck* optical spectroscopy (red solid line) and *NuSTAR* X-ray spectroscopy (cyan filled circles). The optical spectrum has been scaled up to match the flux of the near-IR spectrum in the overlap wavelength region. The optical spectrum from Marchã et al. (1996) (green solid line) is included for comparison. The *Swift* optical/UV magnitudes close in time with the near-IR spectroscopy are shown as the black, filled squares and the best fit to the co-added *Swift* X-ray spectrum as the thick, black solid line. The magenta filled triangles, filled and open squares and open circles indicate the 2MASS, *WISE* and *Spitzer* IRAC infrared photometry and the *Swift* BAT hard X-ray spectrum, respectively. The frequencies of the 10 and 18 μm dust silicate features are indicated by the vertical magenta dotted lines. Right-hand panel: results from a fit of the accretion disc model of Done et al. (2012, 2013) to the binned data (black points) for a non-rotating ($a^\star = 0$) black hole (dashed lines) and a black hole with spin $a^\star = 0.8$ (solid lines) for a fixed mass of $2 \times 10^7 \, M_\odot$. The total accretion disc spectrum including its reprocessed components is shown in black with the individual components as follows: thermal accretion disc spectrum (red), soft Comptonized component (green) and hard Comptonized component (blue). The additional blackbody for the hot dust component is shown as the magenta line.

at the 1σ level. The agreement between black hole mass estimates from the broad emission lines and those from the short-term X-ray variability, which lie in the range of $\sim$1.0–1.7 $\times 10^7$ solar masses, are also in reasonable agreement with each other, although we have used now a completely different method.

There are also other methods that can be used to estimate the black hole mass, which are based on the dispersion instead of the FWHM of the broad emission line (Landt et al. 2013), and the line and X-ray luminosity instead of the ionizing continuum luminosity (Greene et al. 2010; Kim et al. 2010). We have also considered these alternative methods and list the results in Table 2. The relationships based on the line dispersion and X-ray luminosity give results in good agreement with our previous estimates. However, using the line luminosities of Paα, Hα and Hβ, we obtain black hole masses in the range of $\sim$0.6–1.2 $\times 10^7$ solar masses, which are a factor of $\sim$2 smaller than our previous estimates, but closer to those obtained from the X-ray variability.

The black hole mass in the source 1H 0323+342 was previously estimated by other authors. Zhou et al. (2007) used the Hβ line luminosity and 5100 Å continuum luminosity together with the FWHM of Hβ and estimated the black hole mass in the range of $\sim$1–3 $\times 10^7$ solar masses, which is consistent with our results. León Tavares et al. (2014) also used the Hβ line luminosity and 5100 Å continuum luminosity together with the FWHM of Hβ and obtained values in the range of $\sim$0.8–2 $\times 10^7$ solar masses. In addition, they estimated the black hole mass based on the luminosity of the host galaxy bulge and obtained values a factor of $\sim$10 higher ($\sim$3–5 $\times 10^8$ solar masses). This is in line with the well-known discrepancy between the black hole mass estimates for narrow-line Seyfert 1s based on their broad emission lines and based on the bulge luminosity or stellar dispersion of their host galaxies (e.g. Mathur, Kuraszkiewicz & Czerny 2001; Grupe & Mathur 2004; Mathur et al. 2012); for a given black hole mass, narrow-line Seyfert 1s tend to reside in galaxies with more luminous bulges, often pseudo-bulges,

that are most likely gas-rich. Finally, most recently, Yao et al. (2015) estimated the black hole mass based on the short time-scale X-ray variability observed in a *Suzaku* X-ray spectrum from 2009. Based on the normalized excess variance for a 40 ks binning of the 2–4 keV light curve, they get a value of $(0.86^{+0.29}_{-0.27}) \times 10^7$ solar masses using the Ponti et al. (2012) relationship for the reverberation-mapped AGN sample. This value is very similar to our result for the 20 ks binning of the *NuSTAR* light curve and, within the 2σ error range, also consistent with our result for a 40 ks time binning.

4 THE SED

4.1 The Eddington ratio

With a reliable black hole mass estimate in hand, we are now in the position to derive the Eddington ratio L/L_{Edd}, where L is the total luminosity of the accretion disc and L_{Edd} is the luminosity of an accretion disc accreting matter at the Eddington limit for a given black hole mass. For this purpose, we have modelled the observed SED of the source 1H 0323+342 from near-IR to X-ray frequencies (see Fig. 2) using the energy-conserving accretion disc model of Done et al. (2012), which was later revised by Done et al. (2013). In short, the model has three components: (i) a relativistic, geometrically thin, optically thick accretion disc, which emits thermal (blackbody) radiation with a spectrum that includes a colour correction term to account for the fact that the disc is not fully thermalized at all radii, (ii) a soft X-ray excess component attributed to low-temperature, optically thick Comptonization of inner disc photons and (iii) an X-ray power law attributed to high-temperature, optically thin Comptonization. This model is incorporated in the XSPEC analysis package under the name OPTXAGNF. However, it is important to also include an inclination dependence of the accretion disc emission and relativistic corrections such as gravitational redshift.

Table 3. Best-fitting parameter values for the accretion disc model of Done et al. (2012, 2013) assuming a Schwarzschild ($a^\star = 0$) and a Kerr ($a^\star = 0.8$) black hole with a mass of 2×10^7 $M_\odot$.

	$L/L_{\rm Edd}$	$\dot{M}$ ($M_\odot$ yr^{-1})	$\nu L_{\rm acc}$ (erg s^{-1})	$r_{\rm cor}$ ($r_{\rm g}$)	$f_{\rm pl}$	$\nu L_{\rm pl}$ (erg s^{-1})	$T_{\rm dust}$ (K)	$\nu L_{\rm dust}$ (erg s^{-1})	χ_ν^2/dof
	(1)	(2)	(3)	(4)	(5)	(6)	(7)	(8)	(9)
$a^\star = 0$	0.55	0.41	1.86e+45	19	0.5	3.39e+44	1627	1.22e+44	4.92/98
$a^\star = 0.8$	1.00	0.37	3.39e+45	7	0.4	3.15e+44	1717	1.08e+44	4.51/98

Notes. The columns are: (1) Eddington ratio; (2) accretion rate; (3) total accretion disc luminosity for the thermal component; (4) radius of the corona (in gravitational radii); (5) fraction of the power below the coronal radius that is reprocessed into the hard Comptonized component; (6) total luminosity of the hard Comptonized component; (7) blackbody temperature of the hot dust component; (8) total luminosity of the hot dust component; and (9) reduced χ^2 and number of degrees of freedom for the best fit. We fixed the inclination of the accretion disc to an angle of $i = 0°$, the outer radius of the accretion disc to the self-gravity radius and the optical depth of the soft Comptonized component to a value of $\tau = 15$.

These effects are incorporated in the code OPTXCONV, which we have used here.

We have performed the accretion disc fits including the following data; the binned near-IR and optical spectrum, whereby we first subtracted the Fe II emission from the optical spectrum and excluded bins that contained strong emission lines and sampled the Balmer continuum in the blue, the *Swift* UVOT magnitudes from the 2015 epoch with the exception of the *V* magnitude, which falls on a strong emission line, the co-added *Swift* XRT spectrum binned to a minimum of 100 counts per energy bin and the *NuSTAR* spectrum. We have assumed the two cases of a non-rotating Schwarzschild black hole, i.e. a dimensionless spin parameter of $a^\star = 0$ and a rotating Kerr black hole with $a^\star = 0.8$. Furthermore, we have included an additional blackbody in our accretion disc fits in order to simultaneously model the hot dust emission in the near-IR. The resulting best-fitting values for the relevant model parameters are listed in Table 3 and the fits are shown in Fig. 2, right-hand panel. We have fixed three of the free parameters, namely, the accretion disc inclination to an angle of $i = 0°$ (face-on view), the outer radius of the accretion disc to the self-gravity radius and the optical depth of the soft Comptonized component to a value of $\tau = 15$. The assumed accretion disc inclination angle is close to the value range of $i = 4°$–$13°$ recently obtained by Fuhrmann et al. (2016) for the orientation of the radio jet based on the apparent superluminal speeds of individual radio components they see on high-spatial resolution Very Large Baseline Array images. For the optical depth, we have assumed the mean value obtained by Done et al. (2012) for their modelling of the mean optical to X-ray AGN SEDs of Jin et al. (2012).

The most important parameter that we would like to be able to constrain from our SED fitting is spin. This would not only determine the Eddington ratio of the source and so help establish if it is a high accretor as usually found for the class of narrow-line Seyfert 1s, but it would be especially important in this case, since a high black hole spin contrary to the zero spin usually found for radio-quiet narrow-line Seyfert 1s (e.g. Done et al. 2013) might explain why the source 1H 0323+342 has a relativistic jet and so is a strong γ-ray emitter (Done & Jin 2016). Although, it could be that a high spin alone is not a sufficient condition for the production of relativistic jets (Foschini 2016). In the absence of far-UV data, which are generally not available for AGN, the spin value can, in principle, be constrained if a soft X-ray excess is detected. However, the spectral slope of this component and its frequency coverage are important too, since only a very steep soft X-ray excess well-sampled down to the lowest X-ray energies can exclude spin values $a^\star > 0$. In our case, we detect a soft X-ray excess component in the co-added *Swift* spectrum, but its frequency coverage reaches down to only

~ 0.4 keV, which is not low enough to differentiate between zero spin and a spin value up to $a^\star = 0.8$. Therefore, we can constrain the Eddington ratio only to a range of values, namely, $L/L_{\rm Edd} \sim 0.5$–1. However, the model cannot fit the data with spin values of $a^\star > 0.8$, since these solutions strongly overpredict the observed soft X-ray flux. Though we note that these solutions would also be of a super-Eddington nature, in which case, energy conservation may not be appropriate due to losses via strong winds and advection (see e.g. Done & Jin 2016; Jin, Done & Ward 2016). Thus, extremely high spins cannot be ruled out if they are accompanied by the expected strong losses for highly super-Eddington flows.

4.2 The jet contribution

We have interpreted the entire SED from near-IR to hard X-ray frequencies as emission that is unassociated with the radio jet. In particular, the synchrotron jet emission is expected to peak at IR frequencies and the associated inverse Compton emission, which is assumed to dominate at γ-ray frequencies, might be detectable already at hard X-ray frequencies. In Fig. 2, left-hand panel, we plot in addition to our near-IR spectroscopy also the photometry from the Two Micron All-Sky Survey (2MASS; Skrutskie et al. 2006) Point Source Catalogue, the *Wide-field Infrared Survey Explorer* (*WISE*; Wright et al. 2010) all-sky survey and the *Spitzer* Enhanced Imaging Products source list. First, we note that the optical and near-IR spectrum of the source 1H 0323+342 form together a butterfly shape around an inflection point with a rest-frame wavelength of 1 μm, which is typical of radio-quiet AGN and generally interpreted as the sum of emission from the (decreasing) thermal accretion disc spectrum and the (rising) hot dust emission (e.g. Carleton et al. 1987; Glikman, Helfand & White 2006; Landt et al. 2011b). Secondly, no significant variability is detected in the near-IR between our GNIRS spectroscopy and the 2MASS photometry, which was obtained about 17 yr earlier on 1998 January 20. Neither is a strong variability observed in the mid-IR between the *Spitzer* IRAC photometry taken on 2008 September 18 and the *WISE* photometry taken on 2010 February 10/11. This points to a dusty torus origin of the IR emission rather than the synchrotron emission from the relativistic jet, which was what was modelled so far in this frequency range (e.g. Abdo et al. 2009; Paliya et al. 2014; Yao et al. 2015). Finally, the emission upturn evident between the two *WISE* photometry points at the longest wavelengths is most likely due to the fact that they are sampling the two dust silicate features at rest-frame wavelengths of 10 and 18 μm (vertical magenta dotted lines in Fig. 2). A strong emission upturn is often observed between

these two features when in emission rather than in absorption (see, e.g. radio-loud quasars in Landt, Buchanan & Barmby 2010).

The inverse Compton emission from the jet most likely starts to dominate over the accretion disc Comptonized power law at the highest energies sampled by *NuSTAR*. We find that the *NuSTAR* data points at energies $\gtrsim 22$ keV lie significantly above the best-fitting Comptonized power law, which we also found evidenced at a low significance level when fitting the data with a sum of two power laws (see Section 2.3.1). The prominence of the jet is then clearly established at energies $\gtrsim 90$ keV ($\nu \gtrsim 10^{19.2}$ Hz) as shown in Fig. 2, left-hand panel, where we have added the hard X-ray spectrum from the *Swift* Burst Alert Telescope (BAT) 70-month catalogue (Baumgartner et al. 2013) fitted with a single power law. Whereas the averaged *Swift* BAT flux is consistent with the *NuSTAR* data in the frequency range of overlap, excess emission is observed at the high-energy end of the spectrum. A jet dominance of the hard X-rays, and even of X-ray energies as low as a few keV when the source is in a high state, was also reported by Foschini et al. (2009) and Foschini (2012) (see their fig. 1, left-hand panel), who analysed the *INTEGRAL* IBIS and *Swift* XRT and BAT data available at the time. However, we note that the 2–10 keV spectral index of our source is much flatter than that usually expected for the coronal emission of high-Eddington sources (Shemmer et al. 2008; Done et al. 2012). Then, if most of the X-ray emission were from the jet rather than the accretion disc corona, it is surprising that the X-ray variability is so similar to the expectations of coronal variability (see Section 3.2). None the less, this could simply indicate that there is a tight linkage between the corona and the jet. We will explore the jet contribution in detail in a subsequent paper (Kynoch et al., in preparation).

5 SUMMARY AND CONCLUSIONS

We have presented here recent quasi-simultaneous optical and near-IR spectroscopy of high quality (high S/N and moderate spectral resolution) for the source 1H 0323+342, which is the lowest redshift member of the rare class of γ-ray detected narrow-line Seyfert 1s. We have supplemented these observations with a *NuSTAR* X-ray spectrum taken about two years earlier and constrained the black hole mass based on several optical and near-IR broad emission lines as well as the short time-scale X-ray variability. With a reliable black hole mass estimate in hand, we have derived the Eddington ratio based on a detailed spectral fitting of our multiwavelength SED with the accretion disc model of Done et al. Our main results can be summarized as follows.

(i) Our three estimates of the black hole mass based on the ionizing continuum luminosity and the width of the hydrogen broad emission lines Hα, Hβ and Paα give a very small range of values of ~ 1.5–2.2×10^7 solar masses, with an average value of $\sim 2 \times 10^7$ solar masses. This amazing consistency between the three estimates is surprising, given that the relationships which they are based on have uncertainties of the order of ~ 40–50 per cent at the 1σ level.

(ii) We obtain a very good agreement between the black hole mass estimates from the broad emission lines and those from the short-term X-ray variability, which lie in the range of ~ 1.0–1.7×10^7 solar masses. In addition, we have considered alternative methods to estimate the black hole mass, which are based on the dispersion instead of the FWHM of the broad emission line and the line and X-ray luminosity instead of the ionizing continuum luminosity. We find in general a good agreement with our previous estimates, except when using the emission line luminosities.

These give black hole masses in the range of ~ 0.6–1.2×10^7 solar masses, which are a factor of ~ 2 smaller than our other estimates.

(iii) The main aim of our SED fitting is to constrain the spin value, which, in turn, determines the Eddington ratio and so the bolometric luminosity. In agreement with previous studies, we find that, in the absence of far-UV data, the spin value can, in principle, be constrained if a soft X-ray excess is detected. We detect this component in our co-added *Swift* spectrum, but its frequency coverage does not reach low enough to differentiate between zero spin and a spin value up to $a^\star = 0.8$. Therefore, we constrain the Eddington ratio only to a range of values of $L/L_{Edd} \sim 0.5$–1. However, we can exclude spin values of $a^\star > 0.8$ and so a super-Eddington nature of the source, since these solutions strongly overpredict the observed soft X-ray flux.
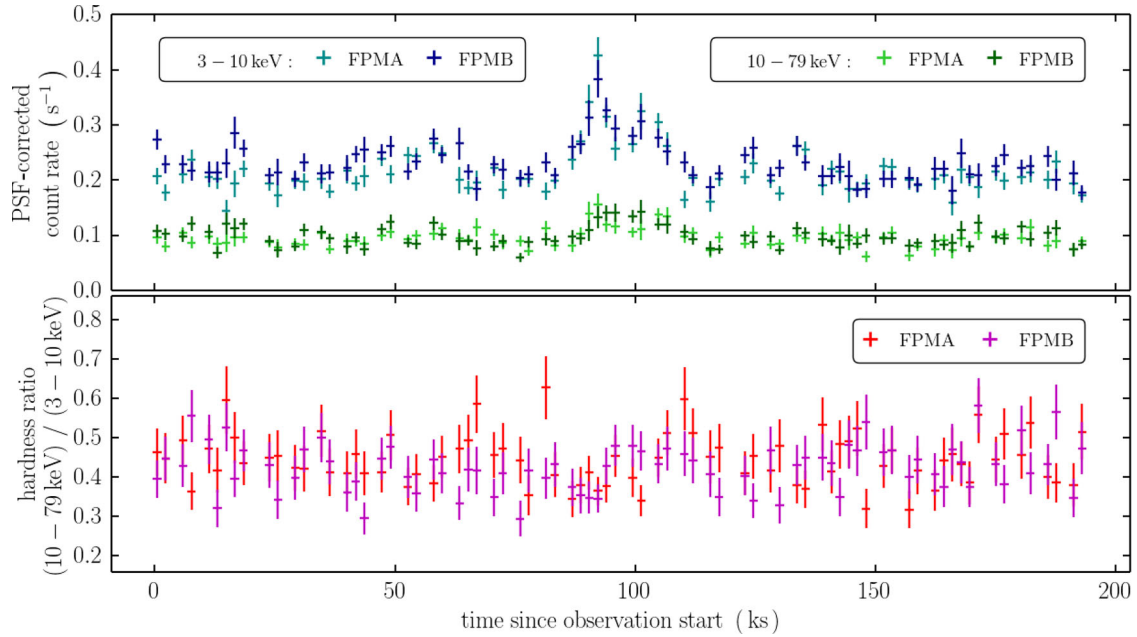
REFERENCES

Abdo A. A. et al., 2009, ApJ, 707, L142
Acero F. et al., 2015, ApJS, 218, 23
Antón S., Browne I. W. A., Marchã M. J., 2008, A&A, 490, 583
Arnaud K. A., 1996, in Jacoby G. H., Barnes J., eds, ASP Conf. Ser. Vol. 101, XSPEC: The First Ten Years. Astron. Soc. Pac., San Francisco, p. 17
Barr P., Mushotzky R. F., 1986, Nature, 320, 421
Baumgartner W. H., Tueller J., Markwardt C. B., Skinner G. K., Barthelmy S., Mushotzky R. F., Evans P. A., Gehrels N., 2013, ApJS, 207, 19
Bentz M. C., Peterson B. M., Netzer H., Pogge R. W., Vestergaard M., 2009, ApJ, 697, 160
Bentz M. C. et al., 2013, ApJ, 767, 149
Berton M., Foschini L., Ciroi S., Cracco V., La Mura G., Di Mille F., Rafanelli P., 2016, A&A, 591, A88
Boroson T. A., Green R. F., 1992, ApJS, 80, 109

Carleton N. P., Elvis M., Fabbiano G., Willner S. P., Lawrence A., Ward M.,
    1987, ApJ, 318, 595
Cooke A., Rodgers B., 2005, in Shopbell P., Britton M., Ebert R., eds, ASP
    Conf. Ser. Vol. 347, Astronomical Data Analysis Software and Systems
    XIV. Astron. Soc. Pac., San Francisco, p. 514
Dickey J. M., Lockman F. J., 1990, ARA&A, 28, 215
Done C., Jin C., 2016, MNRAS, 460, 1716
Done C., Davis S. W., Jin C., Blaes O., Ward M., 2012, MNRAS, 420, 1848
Done C., Jin C., Middleton M., Ward M., 2013, MNRAS, 434, 1955
Elias J. H., Joyce R. R., Liang M., Muller G. P., Hileman E. A., George
    J. R., 2006, in McLean I. S., Iye M., eds, Proc. SPIE Conf. Ser.
    Vol. 6269, Ground-based and Airborne Instrumentation for Astronomy.
    SPIE, Bellingham, p. 62694C
Foschini L., 2012, Proceedings of the Conference 'Nuclei of Seyfert galaxies
    and QSOs - Central Engine & Conditions of Star Formation'. Max-
    Planck-Insitut für Radioastronomie (MPIfR), Bonn, p. 10
Foschini L., 2016, preprint (arXiv:1205.3128)
Foschini L., Maraschi L., Tavecchio F., Ghisellini G., Gliozzi M., Sambruna
    R. M., 2009, Adv. Space Res., 43, 889
Foschini L. et al., 2016, preprint (arXiv:1602.08227)
Fuhrmann L. et al., 2016, preprint (arXiv:1608.03232)
Glikman E., Helfand D. J., White R. L., 2006, ApJ, 640, 579
Green A. R., McHardy I. M., Lehto H. J., 1993, MNRAS, 265, 664
Greene J. E., Ho L. C., 2005, ApJ, 630, 122
Greene J. E. et al., 2010, ApJ, 723, 409
Grupe D., Mathur S., 2004, ApJ, 606, L41
Harrison F. A. et al., 2013, ApJ, 770, 103
Jin C., Ward M., Done C., Gelbord J., 2012, MNRAS, 420, 1825
Jin C., Done C., Ward M., 2016, MNRAS, 455, 691
Kaspi S., Smith P. S., Netzer H., Maoz D., Jannuzi B. T., Giveon U., 2000,
    ApJ, 533, 631
Kim D., Im M., Kim M., 2010, ApJ, 724, 386
Landt H., Bentz M. C., Ward M. J., Elvis M., Peterson B. M., Korista K. T.,
    Karovska M., 2008, ApJS, 174, 282
Landt H., Buchanan C. L., Barmby P., 2010, MNRAS, 408, 1982
Landt H., Bentz M. C., Peterson B. M., Elvis M., Ward M. J., Korista K. T.,
    Karovska M., 2011a, MNRAS, 413, L106
Landt H., Elvis M., Ward M. J., Bentz M. C., Korista K. T., Karovska M.,
    2011b, MNRAS, 414, 218
Landt H., Ward M. J., Peterson B. M., Bentz M. C., Elvis M., Korista K. T.,
    Karovska M., 2013, MNRAS, 432, 113
Landt H., Ward M. J., Elvis M., Karovska M., 2014, MNRAS, 439, 1051

León Tavares J. et al., 2014, ApJ, 795, 58
McHardy I. M., Koerding E., Knigge C., Uttley P., Fender R. P., 2006,
    Nature, 444, 730
Madsen K. K. et al., 2015, ApJS, 220, 8
Magdziarz P., Zdziarski A. A., 1995, MNRAS, 273, 837
Marchã M. J. M., Browne I. W. A., Impey C. D., Smith P. S., 1996, MNRAS,
    281, 425
Massey P., Gronwall C., 1990, ApJ, 358, 344
Mathur S., Kuraszkiewicz J., Czerny B., 2001, New Astron., 6, 321
Mathur S., Fields D., Peterson B. M., Grupe D., 2012, ApJ, 754, 146
Mejía-Restrepo J. E., Trakhtenbrot B., Lira P., Netzer H., Capellupo D. M.,
    2016, MNRAS, 460, 187
Nandra K., George I. M., Mushotzky R. F., Turner T. J., Yaqoob T., 1997,
    ApJ, 476, 70
Oke J. B. et al., 1995, PASP, 107, 375
Onken C. A., Ferrarese L., Merritt D., Peterson B. M., Pogge R. W., Vester-
    gaard M., Wandel A., 2004, ApJ, 615, 645
Paliya V. S., Sahayanathan S., Parker M. L., Fabian A. C., Stalin C. S.,
    Anjum A., Pandey S. B., 2014, ApJ, 789, 143
Peterson B. M., 1993, PASP, 105, 247
Polletta M. et al., 2007, ApJ, 663, 81
Ponti G., Papadakis I., Bianchi S., Guainazzi M., Matt G., Uttley P., Bonilla
    N. F., 2012, A&A, 542, A83
Shemmer O., Brandt W. N., Netzer H., Maiolino R., Kaspi S., 2008, ApJ,
    682, 81
Skrutskie M. F. et al., 2006, AJ, 131, 1163
Vaughan S., Edelson R., Warwick R. S., Uttley P., 2003, MNRAS, 345,
    1271
Véron-Cetty M.-P., Joly M., Véron P., 2004, A&A, 417, 515
Vestergaard M., Peterson B. M., 2005, ApJ, 625, 688
Wandel A., Peterson B. M., Malkan M. A., 1999, ApJ, 526, 579
Wright E. L. et al., 2010, AJ, 140, 1868
Xiao T., Barth A. J., Greene J. E., Ho L. C., Bentz M. C., Ludwig R. R.,
    Jiang Y., 2011, ApJ, 739, 28
Yao S., Yuan W., Komossa S., Grupe D., Fuhrmann L., Liu B., 2015, AJ,
    150, 23
Zhou H. et al., 2007, ApJ, 658, L13

APPENDIX A: *GEMINI* NEAR-IR SPECTRUM, *KECK* OPTICAL SPECTRUM AND *NuSTAR* LIGHT CURVE

Figure A1. *Gemini* GNIRS near-IR spectrum shown as observed flux versus rest-frame wavelength. Emission lines listed in table 4 of Landt et al. (2008) are marked by dotted lines and labelled; black: permitted transitions, green: permitted Fe II multiplets (not labelled), red: forbidden transitions and cyan: forbidden transitions of iron (those of [Fe II] not labelled).

Figure A2. *Keck* LRIS optical spectrum shown as observed flux versus rest-frame wavelength. Emission lines labelled as in Fig. A1.

Figure A3. Top panel: *NuSTAR* light curve in bins of 30 min for the two focal plane modules A (FPMA) and B (FPMB) in the two energy bands 3–10 and 10–79 keV. Bottom panel: the ratio between the count rate in the 10–79 keV band and that in the 3–10 keV band (i.e. the hardness ratio) for the two modules as a function of time. Note that the spectrum did not significantly change during the brief period of increased flux.

This paper has been typeset from a TEX/LATEX file prepared by the author.